Self-assembly, cytocompatibility, and interactions of desmopressin with sodium polystyrene sulfonate

Article

Accepted Version

Self-assembly, Cytocompatibility, and Interactions of Desmopressin with Sodium Polystyrene Sulfonate

Ana B. Caliari[1], Renata N. Bicev[1,2], Caroline C. da Silva[1], Sinval E. G. de Souza[1], Marta G. da Silva[1], Louise E. A. Souza[1], Lucas R. de Mello[1,3], Ian W. Hamley[3], Guacyara Motta[4], Jéril Degrouard[2], Guillaume Tresset[2], Alexandre J. C. Quaresma[1], Clovis R. Nakaie[1], and Emerson R. da Silva[1,*]

[1] Departamento de Biofísica, Universidade Federal de São Paulo, São Paulo 04062-000, Brazil

[2] Université Paris-Saclay, CNRS, Laboratoire de Physique des Solides, 91405 Orsay, France

[3]Department of Chemistry, University of Reading, Reading RG6 6AD, United Kingdom

[4]Departamento de Bioquímica, Universidade Federal de São Paulo, São Paulo 04044-020, Brazil

ABSTRACT

Peptide-polymer systems hold strong potential for applications in nanotherapeutics. Desmopressin, a synthetic analogue of the antidiuretic hormone arginine vasopressin, may serve as a valuable case of study in this context since it is a first-line treatment for disorders affecting water homeostasis, including diabetes insipidus. It also has an established use as a hemostatic agent in von Willebrand disease, and recently, its repurposing has been suggested as a neoadjuvant in the treatment of certain types of cancer. Despite its well-documented medical uses, studies on the supramolecular organization of desmopressin and its association with polymers remain scarce, limiting the therapeutic benefits of these nanostructured arrays. Here, we investigate the self-assembly of desmopressin and its association with sodium polystyrene sulphonate (NaPSS), a potassium-binding polymer used to treat hyperkalemia. Using structural techniques such as small-angle X-ray scattering (SAXS), cryogenic transmission electron microscopy (cryo-TEM), and atomic force microscopy combined with infrared nanospectroscopy (AFM-IR), we identified that desmopressin associates with NaPSS to form hybrid fibrillar nanoassemblies characterized by β-turn enriched domains and the appearance of β-sheet content. *In vitro* cytotoxicity assays conducted on breast cancer cell lines MCF-7 and MDA-MB-231 showed that NaPSS/desmopressin complexes are well-tolerated by the non-metastatic MCF-7 cells while displaying inhibitory effects against the metastatic MDA-MB-231 cells. The findings presented here, which demonstrate the successful association of two drugs already validated for medical use and the ability of the hybrid matrix to modulate cell interactions, potentially contribute to the design of peptide-polymer therapeutic systems.

*Corresponding author: er.silva@unifesp.br

INTRODUCTION:

Peptide-polymer systems potentially combine the advantageous characteristics of synthetic products (e.g., processability and scalability) with the inherent bioactivity and functionalities of physiological proteins.[1,2] However, achieving this potential requires a detailed understanding of the complex interactions that drive supramolecular associations in these hybrid architectures. The antidiuretic hormone (ADH), arginine vasopressin, plays a central role in human physiology by regulating water balance and controlling the amount of urine produced by the kidneys.[3,4] Dysfunction in the ADH system affects water homeostasis, leading to urinary disorders, with major examples being diabetes insipidus and enuresis.[5–7] The first-line medication for diabetes insipidus is desmopressin acetate, a synthetic ADH analog.[8–11] Desmopressin is also largely used for bleeding diseases,[12,13] and more recently, its off-label use has been proposed as a neoadjuvant in certain types, with some studies advancing to phase I/II clinical trials.[14–18]

Desmopressin is formed by a sequence of nine amino acids arranged in a partly cyclized strand,[19] as displayed in Scheme 1a. A disulfide bridge between the thiol group of a 3-mercaptopropionic acid (MPA) at position #1 and a cysteine sidechain at position #6 results in a highly constrained three-dimensional arrangement, showing reduced conformational flexibility (1b) and leading to stronger stability and higher potency compared to native ADH.[9,11]

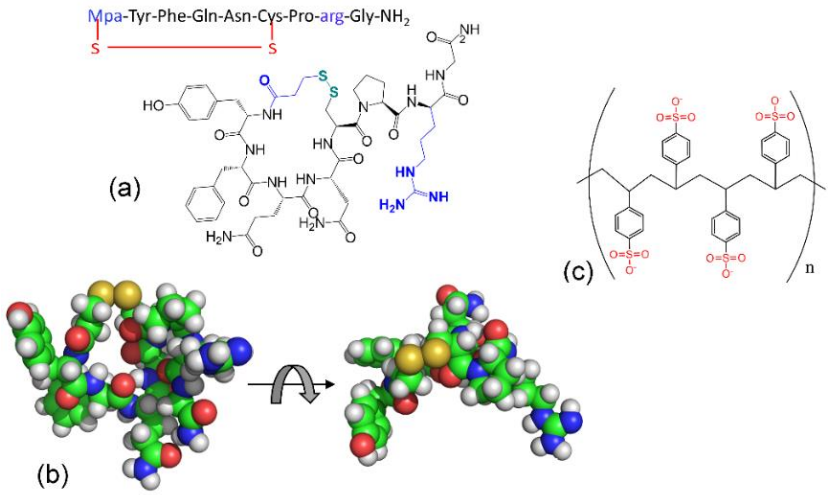

Scheme 1. Structure of desmopressin peptide showing (a) the primary amino acid sequence and its structural formula with the disulfide bridge highlighted in green and the synthetic modifications relative to the antidiuretic hormone marked in blue (MPa = 3-mercaptopropionic acid, arg = D-arginine enantiomer). (b) Three-dimensional arrangement assumed by the sequence, highlighting its cyclization and low flexibility. (c) Structure of polystyrene

sulfonate, with the sulfonate groups (negatively charged at neutral pH) highlighted in red (hydrogens and sodium ions omitted).

Although medical applications of desmopressin have been well-documented during the last decades,[6,8,9,11,20] only a handful of studies are found in the literature reporting the association of this peptide hormone with macromolecular species.[21–24] However, detailed investigations on the self-assembling properties of this peptide in macromolecular systems and the nanoscopic organization of the resulting materials are still lacking, thus hindering potential benefits in the development of nanotherapeutics related to disorders of the vasopressin system.

To fill this gap, we present here an extensive physicochemical investigation on the self-assembly of desmopressin acetate and its association with sodium polystyrene sulfonate (NaPSS). NaPSS is an FDA-approved polymer drug widely used to treat hyperkalemia (i.e., elevated potassium levels in the blood),[25] and since it is a sodium-releasing agent, the combination with desmopressin potentially contributes to mitigate hyponatremia, the most significant side-effect of this peptide.[26] Therefore, the choice of NaPSS as a polymer matrix to form a hybrid system with desmopressin is justified, as this platform consists solely of components that have already been validated for medical use, substantially enhancing the potential of these platforms. Here, we report the discovery that desmopressin forms oligomeric aggregates on its own at sub-millimolar concentrations and associates with NaPSS to form hybrid fibrillar assemblies. We demonstrate a robust association with NaPSS through various structural methods, including synchrotron X-ray scattering (SAXS), cryogenic electron microscopy (cryo-TEM), and atomic force microscopy combined with infrared nanospectroscoy (AFM-IR). The combination of these techniques provides a unique platform for obtaining valuable information at the nanoscale. SAXS is a powerful method to probe the morphology of nanoparticles in liquid media, while cryo-TEM enables direct-space visualization of these aggregates under vitrified conditions, avoiding drying artifacts present in other preparation methods. The major advantage of AFM-IR is its ability to display vibrational data from individual nanoparticles. Remarkably, we show that the association with NaPSS induces the formation of hybrid arrays characterized by β-turn enriched domains and the appearance of β-sheet content. *In vitro* assays conducted on breast tumor models showed that

cytotoxicity of these hybrid assemblies remained minimal to the non-invasive MCF-7 lineage, while exhibiting moderate but significant killing effects against metastatic MDA-MB-231 cells.

MATERIALS AND METHODS

Synthesis of desmopressin acetate: desmopressin, 3-MPA-Tyr-Phe-Gln-Asn-Cys-Pro-(D-Arg)-Gly-NH_2, was manually synthesized using standard Boc approaches.[27–29] The abbreviations of the reagents used in the synthesis read as follows: 3-MPA (3-mercaptoproionic acid), MBHAR (methylbenzhydrylamine-resin), TFA (trifluoroacetic acid), DCM (dichloromethane), DIEA (N,N-diisopropylethylamine), DMF (dimethylformamide), DIC (diisopropylcarbodiimide), HOBt (1-hydroxybenzotriazole), HOAt (1-Hydroxy-7-azabenzotriazole), TBTU (tetramethyluronium tetrafluoroborate), DMSO (dimethyl sulfoxide), NMP (N-methyl-2-pyrrolidone), AcOH (acetic acid), MeOH (methanol), and MeCN (acetonitrile). In the desmopressin sequence, D-Arg represents the D-isomer of arginine, and NH_2 denotes amidation at the C-terminus. Amino acids and resins used in the peptide synthesis were purchased from Sigma Aldrich (Saint Louis, USA). Starting with the C-terminal amino acid coupled to MBHAR, the synthesis was performed through successive α-amino group deprotection and neutralization steps in 30% TFA/DCM (30 min) and 10% DIEA/DCM (10 min), respectively. Amino acid couplings were carried out using DIC/HOBt in DCM/DMF (1:1) and, when necessary, TBTU in the presence of HOBt or HOAt and DIEA in 20% DMSO/NMP. After a coupling period of about 2 hours, qualitative ninhydrin tests were performed to assess the completion of the reaction. The acidic cleavage to remove peptide chains from MBHAR resin was carried out according to previous work introduced in our laboratory.[30] The formation of the disulfide bond between 3-MPA and the cysteine sidechain was conducted in a 10 mM potassium ferrocyanide solution with pH = 6.8, following previously documented methods.[27] The ferrocyanide anion was extracted on an ion exchanger resin AG3-X-4A column. The eluted peptide solution was then evaporated under vacuum and further lyophilized to obtain a white powder product. All solvents used in the synthesis were purchased from Merck (Darmstadt, Germany), had analytical purity grade, and were used as received. **Semi preparative RP-HPLC:** The crude desmopressin powder was purified in a semi-preparative HPLC system consisting of a Waters 2487 detector coupled to a Wat052105 pump. Separation was carried out on a

Prep-PAK 500 column and flow was driven by a Waters Prep LC controller. Solvent A was 1% AcOH in H_2O and solvent B was 90% MeCN in H_2O + 1% AcOH. A linear gradient was applied, which was dependent on the retention time determined in the HPLC analysis performed with the same solvents. The flow rate was kept at 10 mL/min, and detection was carried out at 220 nm. The peptide was obtained in the acetate salt form. **Analytical RP-HPLC**: The purity of the resulting product was determined using a chromatography system consisted of two model 510 HPLC pumps (Waters, Milford, MA, USA), an automated gradient controller, a Rheodyne manual injector, a 486 detector, and a 746 data module. Analyses were performed on a 4.6 × 150 mm C18 column, pore size 300 Å, and particle size 5 μm (Vydac, Hesperia, CA, USA). Solvents A and B were the same as above. A linear gradient of 10-90% solvent B was applied at a flow rate of 1.5 mL/min during 30 min. The purities of the batches used in the current work were at least 97% (see SI file, Fig. S1 for representative chromatograms). **Mass Spectrometry:** The analytical characterization of the purified desmopressin was performed on a LC/ESI-MS equipment consisting of a 2690 Alliance separation module and a 996-photodiode array detector (Waters, Eschborn, Germany). The samples were automatically injected on a C18 Nova-Pak column with 2.1 × 150 mm, 60 Å pore size, and 3.5 μm particle size. Solvents A and B were the same as above. Elution was carried out with a flow rate of 0.4 mL/min using a linear gradient ranging from 5% to 95% B over 30 min. The molecular mass of the resulting product was found to be Mw = 1069.6 g/mol (SI file, Fig. S1c, expected mass 1069.22).

Preparation of desmopressin/NaPSS samples: Poly(sodium 4-styrene sulfonate) (NaPSS) was acquired from Sigma-Aldrich (#243051, M_w~70,000) and used as received. NaPSS stock solutions were prepared by dissolving the polymer in ultrapure water at a concentration of 1 mg.mL^{-1} (~15 μM), whereas desmopressin stocks were prepared at 1 mg·mL^{-1} (~940 μM). Desmopressin stocks were prepared in 10 mM PBS (pH 7.2). Complexes were prepared by mixing appropriate amounts from the stock solutions to achieve the desired concentrations. The mixtures were vigorously vortexed, and the complete dissolution of both the peptide and polymer was confirmed by the clear appearance of the resulting solution. The samples were allowed to equilibrate at room temperature for approximately 2 hours prior to further analysis.

Determination of critical aggregation concentrations (CAC): CAC values were assessed through steady-state fluorimetry experiments performed on a Shimadzu F-2500 fluorimeter. Samples were analyzed at desmopressin concentrations ranging from 10 $\mu g \cdot mL^{-1}$ to 10 $mg \cdot mL^{-1}$ (9.3 nM to 9.3 mM). Two sets of experiments were carried out to investigate the emission behavior of different chromophores in the presence of desmopressin. The first series of samples contained only desmopressin dissolved in buffer, and the assays explored the self-fluorescence of the tyrosine residue in the peptide sequence. Excitation was set at λ_{exc} = 276 nm, and emission spectra were collected in the range 290 nm < λ_{em} < 400 nm. A second series of samples was prepared in desmopressin solutions containing 75 μM ANS (1-anilino-8-naphthalene sulfonate). Excitation was set at λ_{exc} = 356 nm, and emission spectra were recorded in the interval 420 nm < λ_{em} < 650 nm. All experiments were carried out at room temperature, using quartz cuvettes with 1 cm pathlength. Both excitation and emission windows were set at 5 nm, and data collection was performed at a speed of 300 nm/min.

Circular dichroism (CD): circular dichroism assays were carried out on a JASCO 810 spectropolarimeter operating at room temperature. Desmopressin solutions were loaded into quartz cuvettes with 1 mm path length and spectra were collected in the far ultraviolet range, 190 nm < λ < 250 nm, with steps of 1 nm and speed of 100 nm/min. The absorbance channel was also monitored during the measurements, and only data with Abs < 1.5 were considered for further analyses. The spectra were obtained from the average of 5 scans, and background curves (i.e., spectra from buffer solutions collected using the same cuvette) were subtracted. The averaged and background-subtracted spectra were then subjected to FFT filters with a 7-point window to eliminate random noise. To convert the data into ellipticity units, the following formula was used:[36] $[\theta] = (mdeg \times MRW)/(l \times C)$, where $[\theta]$ represents the molar ellipticity in $[deg \cdot cm^2 \cdot cm^{-1}]$ units, *mdeg* is the CD signal in millidegrees, *MRW* is the mean residue weight (here 133 g/mol), *l* is the cuvette path length in mm, and *C* is the sample concentration in $mg \cdot mL^{-1}$.

Quenching assays: The accessibility of the tyrosine chromophore was assessed through fluorescence experiments using acrylamide as a quencher. To this end, desmopressin solutions at a fixed concentration of 0.5 $mg \cdot mL^{-1}$ (0.47 mM, below the CAC) were prepared in buffer, and fluorescence

spectra were recorded during titrations with acrylamide in the range of 0-1.5 mg·mL^{-1} (20 mM). The fluorescence intensities at λ_{em} = 305 nm were used to construct Stern-Volmer plots, which were fitted with the equation $F/F_0 = 1 + K_{SV} \times [Acr]$, where K_{SV} is the Stern-Volmer constant, [Acr] is the quencher concentration, and F/F_0 is the ratio between fluorescence intensities at a given acrylamide concentration and that of the solution without acrylamide. These same conditions were used in experiments exploring tyrosine quenching in desmopressin/polymer mixtures.

Small-angle X-ray scattering (SAXS): SAXS measurements were carried out on the SWING beamline of the SOLEIL synchrotron facilities (Saint Aubin, France). Peptide solutions were prepared at 4 mg·mL^{-1} because this concentration was found to be suitable to get sufficient intensity levels. NaPSS samples were prepared at 1 mg·mL^{-1}. The beamline X-ray energy was 12 keV energy (λ = 1.03 Å) with a beam cross-section of 20 × 200 μm². Data collection was performed using a Dectris Eiger X4M CCD detector, with a pixel size of 75 × 75 μm² and a working area of 162.5 × 155.2 mm². A sample-to-detector distance D_{SD} = 2 m was used to provide access to a q-range in the interval 0.04 nm^{-1} ≤ q ≤ 5.50 nm^{-1}. The experiments were conducted with the BioSAXS setup using an automated system that injected samples from a 96-well plate. Approximately 50 μL of sample were flowed through a 1.5 mm quartz capillary during X-ray illumination. About ten SAXS frames, each of 1 s, were collected during the flow and averaged if no radiation damage was detected, averaging and background subtraction was applied. All measurements were performed at 25 °C, and data analysis was conducted using fitting models from the SASFit program library.[31] Equations and details on fitting models used to extract structural information from SAXS data are described in the SI file (eqs. S1-S5) and the references therein.

Cryo-TEM imaging: Samples for cryogenic transmission electron microscopy were prepared by depositing 5 μL of solutions containing desmopressin, polymers, or a mix of both, onto glow-discharged Quantifoil grids. Lipid vesicles composed of a mix of phosphatidylcholine and fatty acids were also analyzed using the same protocol (see details in the SI file, supplementary methods). Excess solution was removed using filter paper before plunging the grids into liquid ethane using a FEI Vitrobot device. The frozen samples were transferred into a Gatan 626 holder and placed in a JEOL JEM-2010 microscope, at a temperature set at -180 °C. A 200 kV field emission gun was used as the electron

source. Images were recorded at a nominal defocus of 1600 or 2000 nm under low-electron-dose conditions with a Gatan Summit K2 camera. Images were denoised by wavelet filtration in ImageJ software ('A trous filter' plugin, with k1 =20, kn>1 = 0).

Atomic force microscopy combined with infrared spectroscopy (AFM-IR): Samples for AFM analyses were prepared by depositing approximately 10 μL of 1 $mg \cdot mL^{-1}$solutions containing desmopressin (plus PSS) on gold-coated silicon substrates and letting them to dry overnight before analysis. AFM-IR measurements were performed using an Anasys NanoIR2-s microscope with Budget Sensors ContGB-G tips, with the following specifications: 17 μm height, 450 μm length, 17 μm thickness, 25 nm radius, and a force constant of 0.2 N/m. The instrument operated in contact mode, collecting both topography and infrared absorption data from areas of 5 × 5 μm^2 or 10 × 10 μm^2 at a scan rate of 0.5 Hz. Two types of experiments were carried out. In the first type, the AFM tip was positioned on top of single nanoparticles, and infrared pulses covering the 950-1920 cm^{-1} range illuminated the region, obtaining infrared spectra from the area under the tip (~50 nm diameter). The pulse rates were around 180 kHz and the spectra were obtained from 32 averages at a wavenumber resolution of 2 cm^{-1}. In the second type of experiment, the infrared emission was fixed at a wavenumber of interest, and a larger area of the substrate was scanned by the AFM tip to obtain spatially resolved absorption maps.

Cell assays: The cellular assays were conducted to assess potential effects of desmopressin and its supramolecular associations with polymers on cell viability. These assays were performed using breast cancer cell lines, the non-metastatic MCF-7 cells (BCRJ code #0162, batch #001094; ATCC® HTB-22™), and the highly metastatic variant MDA-MB-231 (BCRJ code #0164, batch #001288; ATCC® HTB-28™). The lineages were purchased from BCRJ (Banco de células do Rio de Janeiro, Duque de Caxias, Brazil). Both cell lines were cultivated in Dulbecco's Modified Eagle's Medium (DMEM) containing 5.6 mM glucose (low glucose type), 44.05 mM sodium bicarbonate, 10.49 HEPES, 1.0 mM pyruvate, 10% fetal bovine serum (FBS), 100 $g \cdot mL^{-1}$ penicilin, 100 $U \cdot mL^{-1}$ streptomycin (DMEM/10%FBS), and maintained at 37 °C in 5% CO_2-humidified atmosphere. Mycoplasma testing was performed for the cell lines in the first passage after thawing each vial. All subcultures involved

detaching cells with 0.25% trypsin-EDTA. The experiments consisted in cultivating the cells in the presence of desmopressin, NaPSS, or desmopressin/NaPSS preparations and assessing metabolic viability through resazurin assays. The following concentrations have been used for assessing cell viability: 1000 $\mu g \cdot mL^{-1}$, 500 $\mu g \cdot mL^{-1}$ and 250 $\mu g \cdot mL^{-1}$. For polymer/peptide mixtures, solutions were prepared at 1:1 ratio (e.g., 1000 $\mu g \cdot mL^{-1}$ NaPSS and 1000 $\mu g \cdot mL^{-1}$ desmopressin). Fluorescence measurements of resorufin, resulting from the reduction of resazurin in the mitochondria of viable cells, were carried out on a plate reader with an excitation wavelength of 570 nm and emission detected in the range of 580-590 nm. The assays were carried out in independent triplicates, on two different days, and the results were calculated as the mean ± standard deviation. Statistical analysis was performed using Welch's tests[32] with the data analysis package available in the Microsoft Excel software.

RESULTS AND DISCUSSIONS

Self-aggregation and secondary structure:

We began our investigations on the supramolecular behavior of desmopressin by analyzing its propensity for self-aggregation. To achieve this, we performed different series of fluorometry experiments, exploring either the intrinsic fluorescence of desmopressin or using the extrinsic fluorophore ANS as previously conducted in peptide systems.[33] In Figure 1a, we show fluorescence spectra from desmopressin solutions at various concentrations. Samples were illuminated at λ_{exc} = 275 nm, corresponding to the excitation wavelength of the tyrosine chromophore. The spectra are characterized by an emission peak at ~307 nm, and the emission yield increases with the concentration of desmopressin. To further evaluate the emission yield, we plotted the fluorescence intensity at 307 nm as a function of peptide concentration. This plot, shown in Figure 1b, reveals that tyrosine emission is characterized by two distinct regimes, with a minor intensity increase at lower desmopressin concentrations followed by an onset of strong fluorescence growth near to ~0.3 $mg \cdot mL^{-1}$. The outline of the curve exhibits sigmoidal shape, with an inflexion point identified at ~1 $mg\ mL^{-1}$, which may be interpreted as a critical aggregation concentration (CAC) separating the two fluorescence regimes. The

presence of a CAC is also suggested by yield studies conducted during peptide synthesis, which have shown that cleavage is more efficient in < 1 mg.mL^{-1} solutions (SI File, Table S1 and Figure S3).

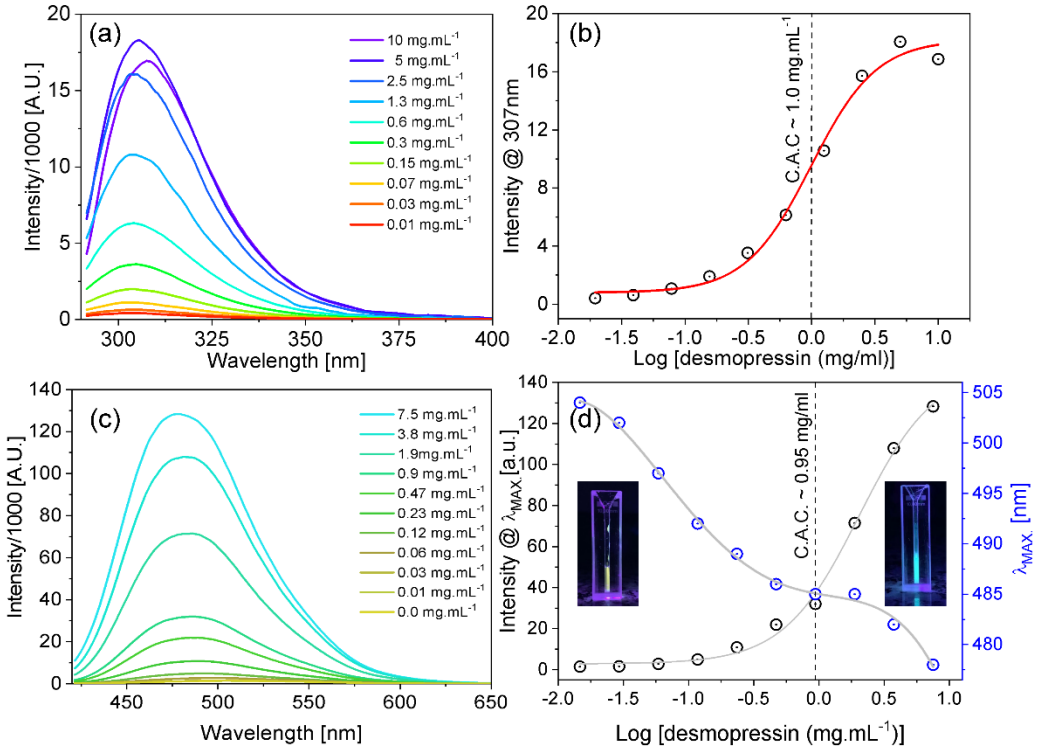

Figure 1. Steady state fluorometry assays. (a) Tyrosine fluorescence spectra of solutions at various desmopressin concentrations (λ_{exc} = 275 nm). (b) Peak intensity of data shown in (a) as a function of the logarithm of desmopressin concentration. The red line represents a fit to the Boltzmann equation. (c) Spectra from desmopressin solutions containing 75 μM ANS (excitation at λ_{exc} = 356 nm). (d) Plots of the peak intensity (black circles) and the peak wavelength (blue circles) as a function of the logarithm of desmopressin concentration. The insets depict the ANS solutions under UV light in mixtures containing the desmopressin below (greenish) and above (vivid turquoise) the CAC.

To independently ascertain the presence of a critical aggregation concentration in desmopressin solutions, we also investigated the fluorescence of ANS in the presence of the peptide. ANS is a fluorophore highly sensitive to the polarity of the surrounding medium.[34] Upon the formation of peptide aggregates, the migration of ANS from the aqueous medium into the hydrophobic clusters leads to an enhancement of fluorescence yield and a blue shift of the emission maximum (see inset in Figure 1d). Therefore, by monitoring either the peak intensity or the wavelength at which it appears, one may examine the formation of supramolecular structures in solution.[33] Figure 1c displays fluorescence spectra from mixtures containing 75 μM ANS and various desmopressin concentrations. It is observed

that the emission yield significantly increases with increasing desmopressin concentrations, thus demonstrating the formation of hydrophobic cores. It should be noted that ANS excitation is carried out at λ_{exc} = 356 nm, a wavelength at which the peptide does not show fluorescence emission, and thus the emission observed in Figure 1c is exclusively attributed to ANS. Additionally, the emission maximum shifts towards lower wavelengths, also supporting the presence of aggregates that host ANS molecules within more hydrophobic surroundings.

The examination of both fluorescence intensity and peak wavelength as a function of desmopressin concentration, shown in Figure 1d, confirms different emission regimes. The fluorescence intensities, displayed by black points in Figure 1d, are significantly enhanced at higher desmopressin concentrations, with an onset near 0.3 $mg.mL^{-1}$, similar to the behavior observed for tyrosine emission. In contrast, the wavelength of the peaks, blue points in Figure 1d, is found to decrease upon desmopressin concentration, crossing over the intensity curve at a concentration of ~0.95 $mg.mL^{-1}$, quite close to the CAC value derived from tyrosine fluorescence assays. The observation of the solutions under UV light, insets in Figure 1d, reveals that when the desmopressin content in the mixture is low, the emission exhibits a greenish glow. However, as peptide concentration surpasses the critical aggregation concentration (CAC), the emission shifts to a vivid turquoise color. Our data demonstrates that the onset of self-assembly occurs at approximately 0.3 $mg.mL^{-1}$, with a distinct transition between fluorescence regimes near 1 $mg.mL^{-1}$. As will be elucidated below, these aggregates are very small, corresponding to arrangements containing only a few desmopressin chains. It should be noted that, given that aggregation phenomena are highly complex and involve multiple sensitive parameters that can vary slightly and impact the critical threshold, the CAC values above must be regarded as approximate estimates for the onset of desmopressin aggregation.

The next step to investigate the structural characteristics of desmopressin was to analyze the secondary structure through circular dichroism (CD). In Figure 2a, CD spectra from peptide solutions at different concentrations feature a strong positive peak centered at 225 nm, which can be attributed to $n \rightarrow \pi^*$ transitions in the aromatic residues Y and F.[35] The consistent intensity of this band, regardless of concentration, suggests that these groups remain unaffected upon interactions between adjacent

desmopressin strands. In contrast, bands appearing at lower wavelengths are highly concentration-dependent, denoting significant changes in the secondary structure upon aggregation.

The CD signature of a 0.1 $mg \cdot mL^{-1}$ peptide solution, a concentration below the self-assembly onset, is characterized by a strong negative rotation at 191 nm (black curve in Figure 2a). This peak can be ascribed to $\pi \rightarrow \pi^*$ transitions in the peptide bond.[36] Given the partially cyclized structure of desmopressin, this band may tentatively indicate turns or random coil conformations. This interpretation is consistent with previous NMR studies which found that the macrocycle of desmopressin is arranged into turns while the acyclic tripeptide tail remains flexible in solution.[37,38] In preparations containing peptides at 0.3 $mg \cdot mL^{-1}$, near the aggregation onset, the spectrum red shifts by about 10 nm, indicating transformations in the secondary structure (red curve). The presence of a positive shoulder near 187 nm, alongside a negative band at 200 nm, makes this spectrum similar to the CD signature of peptides conformed into type II β-turns.[39] Finally, considering data from solutions containing higher desmopressin concentrations, 10 $mg \cdot mL^{-1}$, the CD spectra are characterized by a negative rotation at 210 nm, which might suggest the emergence of β-sheet structures in solution.[40] The formation of β-sheet structures is also suggested by thioflavin T (ThT) fluorescence assays, which are sensitive to these secondary-structure conformations and widely used to identify amyloid aggregates.[34,41] ThT intercalates into the grooves formed by adjacent peptide strands, leading to the stabilization of its rotational degrees of freedom, and a significant enhancement of fluorescence yield.[42] Figure 2b shows ThT fluorescence spectra from solutions containing desmopressin at concentrations below and above the CAC. It can be observed that in samples prepared at 3 $mg \cdot mL^{-1}$, a concentration above the aggregation onset, ThT emission is around 5 times higher than in solutions without peptides, hinting at β-sheet aggregates, consistent with CD data shown in 2a that also suggested the emergence of β-sheets at higher concentrations.

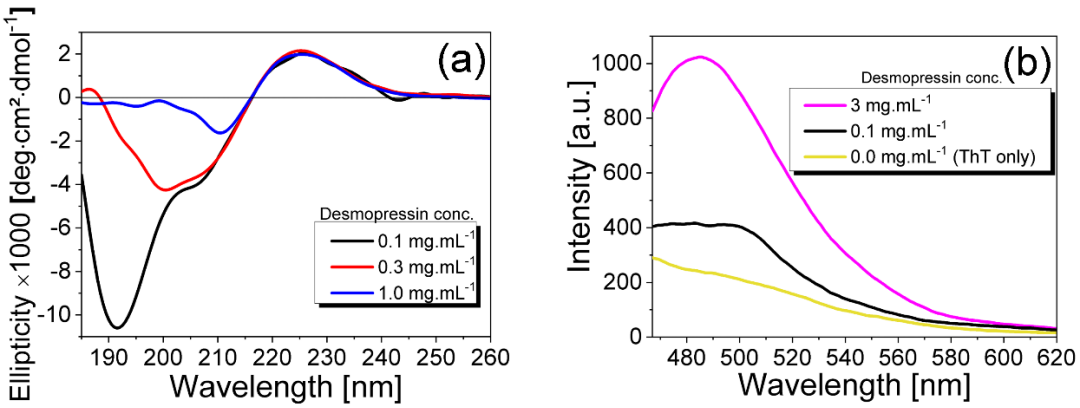

Figure 2. (a) CD spectra from desmopressin solutions at concentrations below and above the CAC. (b) Fluorescence profiles of 30 μM thiflavin T (ThT) in mixtures containing desmopressin at the indicated concentrations. The enhancement in ThT emission indicates the formation of amyloid-like β-sheet cores.

Interaction with Sodium Polystyrene Sulfonate in Solution:

We next evaluated the interactions between desmopressin and sodium polystyrene sulfonate (NaPSS) in solution. NaPSS has cation-binding capabilities, provided by the sulfonate groups along the polymer, which offer interaction sites for desmopressin through electrostatic association with the arginine side chain (see groups highlighted in blue and red in the structures of desmopressin and NaPSS shown in Scheme 1). This characteristic, along with similarities in ionic strengh in nucleic acid strands, has made polystyrene sulfonate polymers and their derivatives successful models for investigating the interplay between capsid proteins and anionic biopolymers.[43–45]

In Figure 3a, Stern-Volmer plots are shown where the fluorescence of tyrosine was monitored upon the addition of acrylamide. Acrylamide is a very effective quencher, and here its addition to solutions containing desmopressin allows us to evaluate the accessibility of the tyrosine residue under different physicochemical conditions. From these plots, we can observe that in the presence of NaPSS at concentrations with a 10:1 excess of sulfonate negative charges (triangles in Figure 3a), the suppression of tyrosine emission is much more effective compared to preparations where desmopressin is alone in solution (squares in Figure 3a). Fits according to the Stern-Volmer equation indicate K_{SV} constants of 0.38 and 0.25 mg·mL^{-1} in the presence and absence of NaPSS, respectively. Therefore, these observations indicate that desmopressin not only interacts with NaPSS but, importantly, such

interactions lead to a spatial arrangement where the tyrosine residues are accessible at external interfaces. This behavior is opposite to what we observe in preparations where desmopressin was placed in the presence of lipid vesicles composed of a mix of phosphatydilcholine and fatty acids (see SI file supplementary methods and Figure S2). In this case, fluorescence suppression is less effective, with a K_{SV} = 0.15 mg·mL^{-1}, indicating that desmopressin is partially buried in the hydrophobic interior of the membranes (black circles in Figure 3a).

In order to probe the induction of spatial order through desmopressin-NaPSS interactions, we further investigated the fluorescence behavior of ThT in peptide/polymer mixtures. In Figure 3b, it is observed that NaPSS is capable of intercalating ThT molecules, leading to ~20-fold increase in the emission yield of this fluorophore (red line in Figure 3b). In contrast, in mixtures where desmopressin and NaPSS appear together, the increase in emission yield is ~100 times greater compared to ThT fluorescence alone in solution (blue line). For comparison, similiar assays conducted in the presence of lipid membranes show a decrease in ThT, suggesting that in the absence of the linear order provided by polymer chains, desmopressin is unable to orient the fluorophore (SI file, Figure S4). CD data also show that the association between the peptide and polymer leads to significant transformations at the secondary structure level. In Figure 3c, CD spectra obtained from a desmopressin solution titrated with NaPSS reveal a transition from random coil conformations to ordered assemblies enriched in β-turns. This is demonstrated by the disappearance of the negative rotation at 193 nm and the emergence of a strong positive band at 187 nm. Additionally, the appearance of negative bands near 206 nm suggests the formation of some β-sheet content. This CD signature is consistent with the 100-fold increase in ThT emission found in desmopressin/NaPSS mixtures and correlates with the formation of organized arrangements displaying β-sheet conformations. It is also consistent with the cryo-EM observations shown below. In addition, the structuring behavior of NaPSS in mixtures with desmopressin contrasts with samples prepared with protamine, a highly cationic peptide with strong solubility that does not form self-assemblies and maintains a random coil conformation even in the presence of the polymer (see SI file, Figure S5).

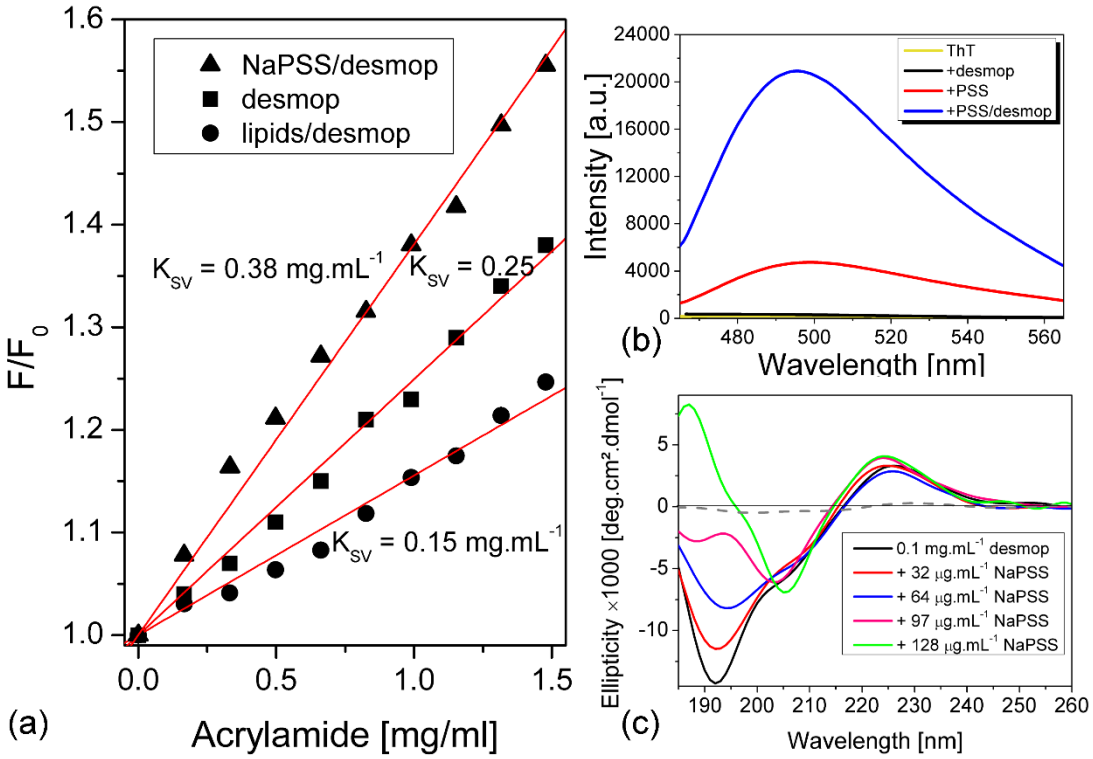

Figure 3. (a) Stern-Volmer plots showing the quenching of tyrosine emission upon titration with acrylamide. Samples contained 0.5 mg·mL^{-1} desmopressin, either alone or in the presence of 1 mg·mL^{-1} NaPSS. The K_{SV} values were obtained from the slope of the linear fits (red lines). (b) ThT fluorescence (30 μM) in mixtures containing 1 mg·mL^{-1} NaPSS (red line) or 1 mg·mL^{-1} NaPSS and 0.5 mg·mL^{-1} desmopressin (blue line). The spectrum of a 0.5 mg·mL^{-1} desmopressin sample is shown as a control. (c) CD spectra of a 0.1 mg·mL^{-1} desmopressin solution titrated with increasing NaPSS concentrations. The dashed grey line is the spectrum of a polymer solution with the same concentration used in the last titration.

The nanoscopic structure of desmopressin/NaPSS aggregates was evaluated through cryo-EM imaging and in-solution SAXS. In Figure 4, a panel with micrographs obtained from vitrified specimens indicates morphological changes in the structures due to the interaction of the peptide with the polymer. Figure 4a shows that in samples containing 4 mg·mL^{-1} desmopressin, a few large aggregates appear with variable dimensions in the range of a few tens of nanometers (white dashed circles in Figure 4a). These aggregates result from the self-assembly revealed by fluorimetry assays above, and they correspond to hydrophobic cores within which ANS fluorescence is enhanced. In contrast, images of desmopressin/NaPSS solutions display irregular assemblies, with elongated dimensions reaching several hundred nanometers in length. These structures, outlined by dashed boxes in Figure 4b, have an appearance consistent with fragments of polymeric films.

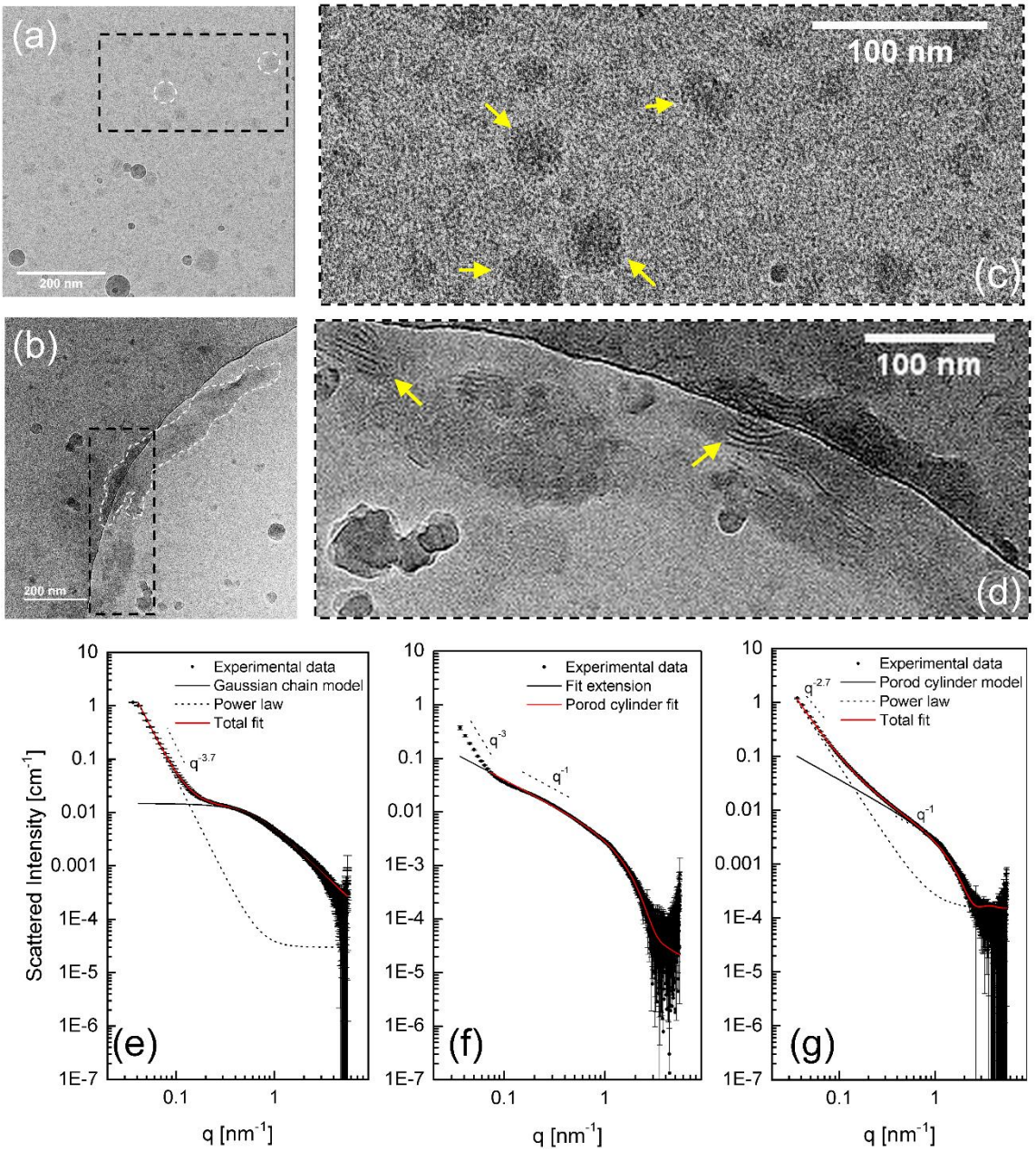

Figure 4. Top row: cryo-EM images obtained from vitrified solutions. (a) Micrograph of a concentrated desmopressin sample (4 mg·mL^{-1}) featuring large globular aggregates with sizes on the order of 40 nm (white dashed circles). (b) Desmopressin/NaPSS mixture (both at 0.5 mg·mL^{-1}) exhibiting large irregular assemblies resembling polymer films (dashed box). In (c) and (d), magnifications of the previous micrographs are shown (black dashed box). In (c), tiny globules, with sizes on the order of a few nanometers corresponding to desmopressin oligomers, can be distinguished, indicated by yellow arrows. In (d), fibrillar structures with diameters on the order of 2.5 nm positioned side by side are observed. Bottom row: SAXS measurements from: (e) concentrated desmopressin solutions (4 mg·mL^{-1}), (f) NaPSS at 1 mg·mL^{-1}, and (g) desmopressin/NaPSS mixtures (both at 1 mg·mL^{-1}).

At closer inspection, Figures 4c and d, nanoparticles can be observed in greater detail. In the case of desmopressin solutions, one can discriminate the aggregates with globular shape indicated by

yellow arrows in Figure 4c. In desmopressin/NaPSS mixtures, Figure 4d, the emergence of elongated arrangements positioned side by side can be distinguished. The diameters of these structures are on the order of 2.5 nm, and their lengths reach several tens of nanometers. The appearance of extended structures, along with the fluorescence increase observed in ThT emission assays and the emergence of β-sheet signatures in CD experiments shown in Figures 3b and c, provides further evidence for ordered structures comprised of polymer chains intercalated with layers of desmopressin molecules.

SAXS data also provided valuable information about the nanoscopic arrangements in solution. In Figures 4e-g, scattering curves indicate a strong dependence on sample composition undoubtedly attesting the presence of different polymorphs in solution. In concentrated desmopressin solutions, the SAXS profile features by a power law in the low-angle region scaling with q^{-4}. This profile is consistent with Porod interfaces,[46,47] indicating large objects whose dimensions are outside the resolution window used in the SAXS experiments and agreeing with the presence of aggregates revealed by cryo-EM data. At intermediate q-range, the data are featured by a plateau followed by a steep descent at the high-q range. This profile is characteristic of Gaussian chains,[46,48] and it is likely a result of the contribution of free desmopressin monomers. To fit the data, we used a combination of the generalized Gaussian chain model[46] that accounts for the high-q range plus a power law to describe the low-angle region. The fitting parameters, summarized in Table 1, indicate a gyration radius of R_g = 1.0 nm and a Flory exponent of ν = 0.63, consistent with swollen coils (Figure 4c). The power law exponent was found to be α = 4.0, compatible with Porod interfaces.[47]

Table 1. SAXS model fitting summary: R_g: gyration radius, ν: Flory exponent, R: Porod cylinder radius, α: scaling exponent.

Sample	Fitting model	Parameters
Desmop (4 mg·mL^{-1})	Gaussian coil + power law	R_g = 2.31 ± 0.04 nm, υ = 0.55 α = 3.7
NaPSS (1 mg·mL^{-1})	Porod cylinder	R = 0.83 ± 0.32 nm
NaPSS (0.5 mg·mL^{-1}) + desmop (0.5 mg·mL^{-1})	Porod cylinder + power law	R = 1.35 ± 0.10 nm α = 2.7

In the case of scattering data from solutions containing NaPSS, the profiles are quite distinct. In samples containing only 1 mg·mL^{-1} NaPSS, Figure 4F, it is observed that in the intermediate q-range the intensity decays with a characteristic exponent of -1, suggestive of elongated structures at size scales of

a few nanometers.[46,49] Doubling the polymer concentration compared to cryo-TEM aimed to improve the signal-to-noise ratio in SAXS assays, while minimizing changes to the chain states between experiments. Data from these samples were satisfactorily fitted with a Porod cylinder form factor,[46] revealing cylinders with a radius $R = 0.83 \pm 0.32$ nm, which can be interpreted as compatible with the cross-section of polymer chains. The low-angle profile of these samples is characterized by a Porod region with a slope of -3, indicative of collapsed chains in interconnected networks forming compact fractal arrangements, consistent with flexibility of NaPSS chains.[49] Finally, in Figure 4G, it is observed that the mixture of desmopressin in a medium containing NaPSS substantially alters the scattering profile, indicating the appearance of new polymorphs in the medium. In particular, it is verified that the decay according to a power law extends over a much larger range of q-values, providing support for the reorganization of the polymer network. The fitting of desmopressin/NaPSS mixture data was performed using a combination of the Porod cylinder form factor and a scaling law, which led to the identification of radii $R = 1.37 \pm 0.10$ nm and scaling exponents of -2.7. The increase in the diameter of the chains compared to the solution containing only NaPSS suggests the formation of a peptide shell resulting from the condensation of desmopressin along the polymer chains. Additionally, the intensity scalingexponent -2.7 suggests branching of chain clusters,[46,49] further confirming that the behavior of NaPSS is significantly affected by interaction with desmopressin.

AFM-IR Examination of Desmopressin/NaPSS Nanoassemblies:

We examined the desmopressin/NaPSS nanoassemblies through atomic force microscopy combined with infrared spectroscopy (AFM-IR).[50,51] AFM-IR is an emerging technique in biophysics, finding applications in a variety of systems, from peptide and nucleic acid analysis to whole cells.[33,48,52–54] It has been also increasingly used in materials science for the chemical characterization of polymer materials.[50] The main advantage of this technique is the ability to simultaneously obtain topography and vibrational data with spatial resolution situated at the nanoscale. These features allow the collection of infrared spectra from individual nanoparticles or the generation of absorbance maps at specific wavelengths. In Figure 5, we present AFM-IR data obtained from a desmopressin sample deposited on

a gold substrate. The topographic image (Figure 5a) shows the formation of a peptide film with average thicknesses around 70 nm (SI Figure S6b). In some areas of the film, small lumps with dimensions of a few tens of nanometers can be distinguished. Figure 5b displays infrared spectra collected at different points of the peptide film. The spectra are characterized by three main resonances located at 1669, 1274, and 1028 cm^{-1}. The peak in the middle of the amide I band, at 1669 cm^{-1}, is characteristic of β-turn conformations, while the intense resonance at 1274 cm^{-1} can tentatively be attributed to the C-O stretching of the tyrosine side chains.[55,56] The resonance at 1028 cm^{-1} is consistent with the stretching of C=O groups in the peptide backbone.[55] Other relatively intense vibrations observed at 1282, 1091, and 1063 cm^{-1} are difficult to attribute unequivocally; however, they are compatible with vibrations reported in the literature for the C-N group: bending (1282 cm^{-1}) and stretching (1091 and 1063 cm^{-1}).[55]

In Figures 5c and 5d, AFM-IR data from a NaPSS sample are presented. The topography data reveals an intricate pattern of crystallized polymer across the surface, forming branched regions. The heights found across the surface are situated in the 30-40 nm range (SI file, Figure S6d), indicating the presence of thin polymer films. At higher levels of detail, it is possible to clearly distinguish polymer grains (SI file, Figure S7). Infrared spectra collected at different points of the substrate, Figure 6b, reveal a set of strong vibrations in the 1000-1200 cm^{-1} range, arising from resonances in the sulfonated benzene groups across the polystyrene chain. Major peaks are found at 1120, 1042, and 1010 cm^{-1}. The bands at 1042 and 1010 cm^{-1} can be assigned to the symmetric stretching of SO_3^- groups and in-plane bending vibrations of benzene rings, respectively.[57] The peak at 1120 cm^{-1} is found in polystyrene sulfonates arranged in syndiotactic configurations.[57,58]

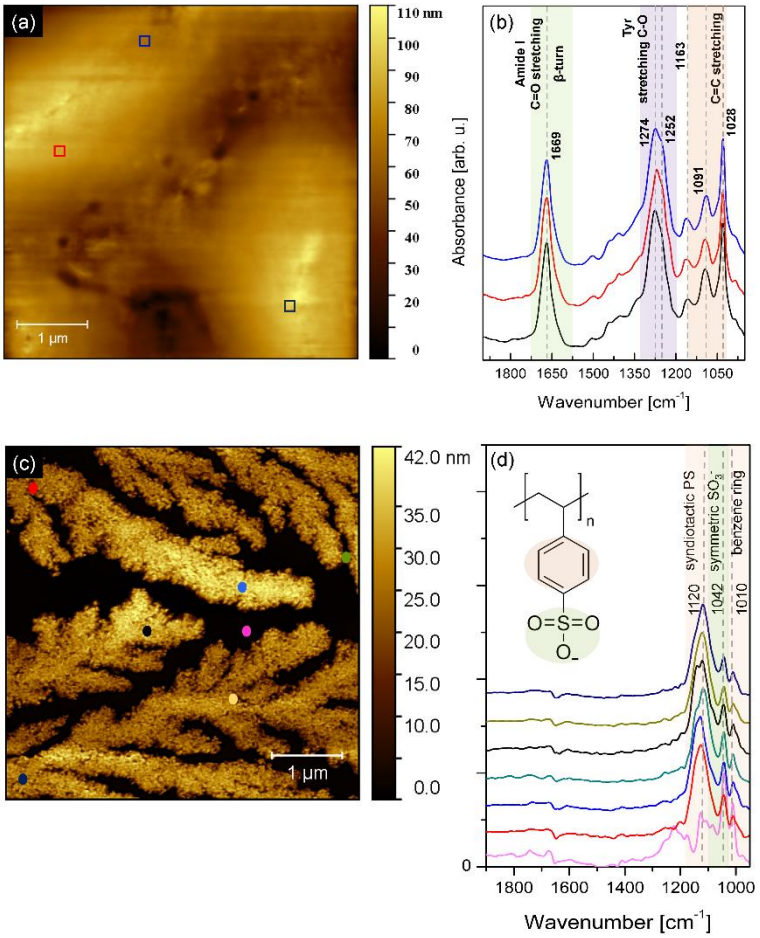

Figure 5. Top row: AFM-IR data of desmopressin samples deposited on gold substrates: (a) Topography image from a desmopressin film dried from a 1 mg·mL^{-1} solution. (b) infrared spectra from the regions indicated in the topography image featuring three major resonances at 1669, 1274, and 1028 cm^{-1}. Bottom row: AFM-IR data of a NaPSS sample dried from a 1 mg·mL^{-1} solution: (c) Topography image showing polymer crystallization at the solid surface. (d) Infrared data highlighting characteristic vibrations, mostly related to sulfonation of the benzene ring, in the 1000-1200 cm^{-1} range.

AFM-IR data from desmopressin/NaPSS mixtures are presented in Figure 6. The topography image clearly indicates morphological changes upon association between the peptide and polymer. Elongated structures resembling bundles of fibers coexist with lumps (Figure 6a). The heights of the lumps reach approximately 60-70 nm, while the average height of the fibers is approximately 30 nm (SI file, Figure 5f). In contrast to the desmopressin and NaPSS samples presented above, the infrared spectra from desmopressin/NaPSS mixtures exhibit numerous peaks (Figure 6b), thus indicating higher complexity in the chemical bonding landscape. Two main sets of peaks can be identified in the spectra: one in the 1600-1700 cm^{-1} range, corresponding to the amide I band, and another one in the 900-1300 cm^{-1} region. The amide I range features an intense resonance at 1675 cm^{-1}, likely representing a blue

shift of the *β*-turn band found at 1669 cm^{-1} in the desmopressin spectra (see Figure 6b). The shift of this resonance toward shorter wavelengths may indicate stronger chemical bonds resulting from the reorganization of desmopressin chains during self-assembly. Additionally, 1675 cm^{-1} corresponds to the lower extreme of the range where β-turn resonances typically appear in the infrared signature of proteins.[55] The emergence of β-sheet content is also suggested by shoulders observed at approximately 1620 cm^{-1}.[56]

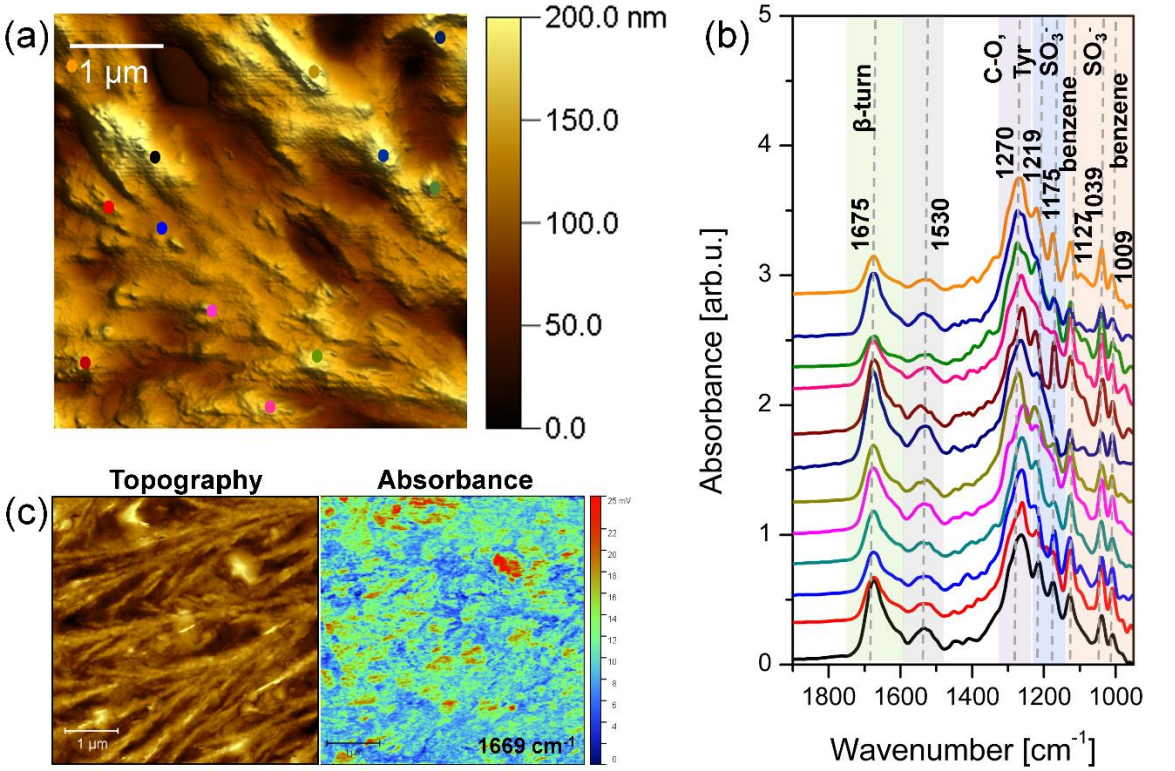

Figure 6. AFM-IR data showing both topography and infrared absorbance data of films dried from desmopressin/NaPSS mixtures. In (a), the topography image reveals that upon mixing with desmopressin, NaPSS forms elongated bundles co-existing with lumps. In (b), infrared spectra exhibit complex vibration profiles, including vibrations associated with polymer groups (1000-1200 cm^{-1} range) and peptide characteristic amide I bands (1600-1700 cm^{-1}), as well as new bands in the range 1200-1300 cm^{-1}associated with desmopressin-NaPSS interactions. (c) topography and absorbance map at 1669 cm^{-1} of NaPSS/desmopressin bundles.

On the other side of the spectra, bands related to the sulfonated benzene group are easily recognized. In addition to peaks already identified in samples containing only NaPSS (see Figure 6b), a sharp band now appears at 1175 cm^{-1}. This peak can be associated with stretching in the sulfonate group and it is widely used to identify sulfonation during NaPSS synthesis.[58] Its appearance in desmopressin/NaPSS samples reinforces the notion that sulfonate groups are privileged binding sites for

desmopressin. Another peak associated with the configuration of polymer side chains appears at 1127 cm^{-1}, blue-shifted regarding spectra from samples containing only NaPSS, where it appears at 1120 cm^{-1} (see Figure 6b). Peaks at 1270 cm^{-1} and 1219 cm^{-1} can be tentatively assigned to the tyrosine side chain and N-H bending, respectively.[55] A prominent role of N-H groups is further suggested by the emergence of vibrations at 1530 cm^{-1} in the amide II band, also corresponding to their bending mode.[55] Putting the findings above together, the infrared data corroborate that the association between desmopressin and polystyrene sulfonate leads to an increase in order and gives raise to new levels of organization in the hybrid arrangements. A comparison of averaged infrared spectra is presented in Figure S8, highlighting the emergence of peaks related to N-H bending and SO_3 stretching, emphasizing the significance of these groups as key sites mediating the association between NaPSS and desmopressin.

We also constructed chemical maps of the samples by plotting the surface absorbance at the wavenumber 1669 cm^{-1}, associated with β-turn conformations in desmopressin.[55] Therefore, through inspection of absorbance maps obtained at this wavelength, we should be able to discriminate the spatial distribution of the peptide within the sample. In Figure 6c, topography data is presented alongside the corresponding absorbance map, highlighting the fibrillar morphology of desmopressin/NaPSS aggregates and revealing heterogeneity across the sample. It can be observed that the absorbance associated with the peptide is dispersed within the fibers, suggesting that desmopressin domains are incorporated into the polymer matrix. Additionally, the chemical map indicates that most of the lumps observed in the topography image also display strong absorbance at 1669 cm^{-1}, thus suggesting enrichment in desmopressin.

Considering the amino acid composition of desmopressin and structural information derived from spectroscopy, microscopy, and scattering assays above, we may now propose some mechanistic insights into both desmopressin self-aggregation and its association with NaPSS. The key steps of self-assembly are illustrated in Figure 7. In the case of desmopressin aggregates (Fig. 7a), the process starts with free peptide chains in solution, surrounded by water layers and neutralized by acetate anions. The presence of nonpolar residues in the desmopressin sequence (phenylalanine, proline) imparts amphiphilic behavior to the peptide, making the hydrophobic effect a major factor contributing to self-

assembly (step 2). Another parameter known to play a relevant role in peptide self-assembly is desolvation,[59] where the release of water molecules from solvation layers provides an entropy gain that stabilizes the aggregates thermodynamically.[60] Finally, as peptide strands hold together, short-range interactions such as H-bonding and π-π stacking may increase structural order within the aggregates (step 3).[61,62]

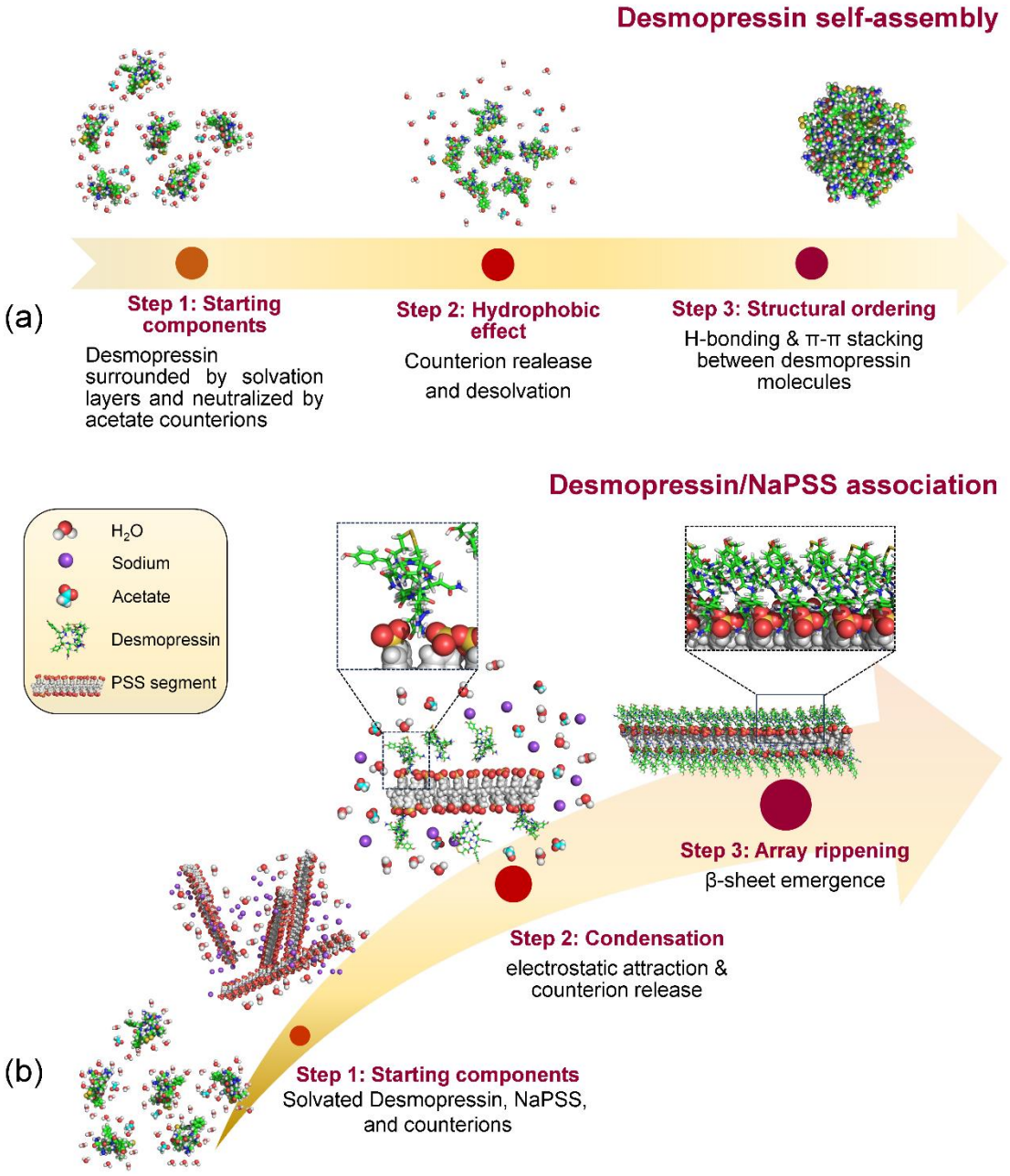

Figure 7. Schematic illustration (not to scale) showing key steps involved in the mechanisms of (a) desmopressin self-aggregation and (b) desmopressin/NaPSS association. The molecular models were arranged manually using Pymol® software.

In the case of desmopressin/NaPSS association (Figure 7b), the process is triggered by electrostatic attraction between oppositely charged sites on the arginine sidechain of desmopressin and sulfonate groups on NaPSS chains (see detail in step 2). Initially, these species are solvated by water shells and their respective counterions. Upon dissociation of counterions from their macromolecular species, desmopressin strands are attracted to the polymer surface. Here, disruption of solvation layers and release of counterions, especially Na^+ ions from polystyrene sulfonate chains, leads to an entropy gain that further stabilizes the assembly. Finally, the pairing of desmopressin molecules along polymer strands enhances order and may promote β-sheet formation, as supported by CD and fluorimetry assays.[62]

Cytotoxicity assays:

We examined the interaction of desmopressin/NaPSS complexes with cell lines *in vitro*. Inspired by reports that identified inhibiting capabilities of desmopressin against tumor cells,[14–16,18,63] we performed resazurin metabolic assays with two breast cancer lineages: the non-metastatic MCF-7 tumor cells and the metastatic MDA-MB-231 lineage. Although the anticancer activity of desmopressin is rather associated with its agonistic activity for clotting factors, resulting in inhibition of tumor vascularization and colonization, *in vitro* assays conducted in culture medium have provided insights into the action of this peptide in carcinogenesis.[15,24,64] The cell lines investigated here are epithelial cells from human origin and are widely used as cell models in the investigation of breast cancer.[65,66] Therefore, the simultaneous evaluation of metabolic effects in these lineages provides a unique opportunity for comparing the interaction of desmopressin/NaPSS formulations in tumor cells with distinct levels of aggressiveness.

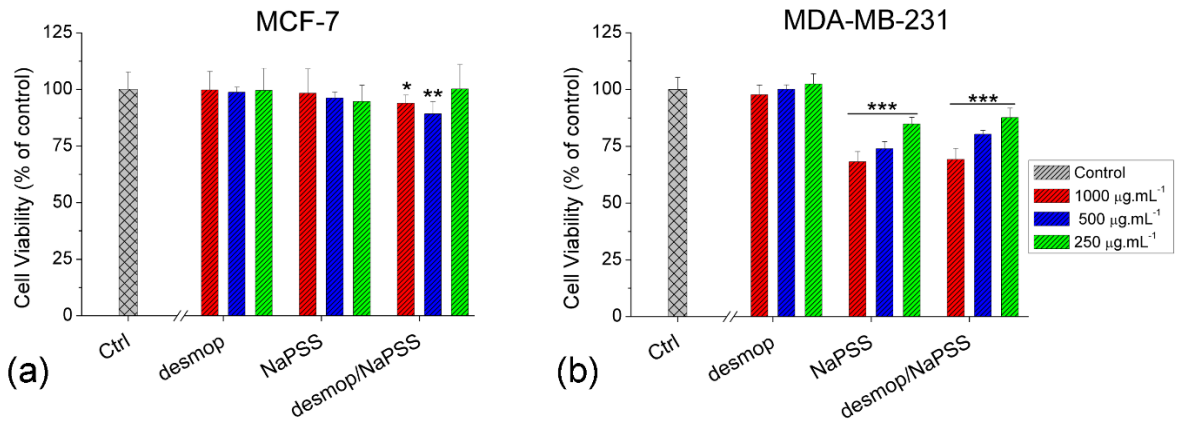

Figure 8. Resazurin cell viability assays of (a) MCF-7 and (b) MDA-MB-231 cells incubated with different concentrations of desmopressin, NaPSS, or desmopressin/NaPSS. In samples incubated with complexes, peptide concentrations are indicated. Significance levels: * $p < 0.05$, ** $p < 0.01$, *** $p < 0.001$ compared with the corresponding negative control (Welch's *t*-tests). Data are presented as mean ± S.D. of 6 measurements (18 for controls). Experiments were performed independently in triplicates on two different days (raw data shown in Table S2).

In Figure 8, the resazurin assays showed no significant metabolic inhibition by desmopressin alone (desmop) compared to the corresponding controls in both cell lines. In contrast, when cells were incubated with NaPSS, distinct behaviors were observed depending on the lineage investigated, with the polymer being tolerated by MCF-7 cells and exhibiting a moderate but significant inhibition against MDA-MB-231 cells. At the highest NaPSS concentration, the viability of metastatic cells decreased to about 70% compared to controls, an effect not observed in MCF-7 cells. In mixtures containing desmopressin/NaPSS nanoassemblies, distinct behaviors were observed comparing both cell lines. The highest concentrations of desmopressin/NaPSS exhibited some toxicity effects against MCF-7 cells, decreasing viability to about 90% of the control. In contrast, the effect on MDA-MB-231 cells was significantly stronger, following the same trend observed in cells incubated with NaPSS. Overall, the results suggest that the combination of desmopressin with NaPSS forms complexes that are well tolerated by non-invasive cells while exhibiting a killing capacity against metastatic cells.

A hypothesis to explain the higher sensitivity of MDA-MB-231 cells to desmopressin/NaPSS complexes may be related to the typically more accelerated metabolism that metastatic cells exhibit compared to non-metastatic cells.[67] In this case, under metabolic stress induced by the presence of desmopressin/NaPSS complexes, they would also exhibit higher rates of cell death, irrespective of the

detailed mechanisms cooperating to cell death. In addition, the plasma membranes in metastatic cells are more fluid and softer, also displaying more membrane protrusions than their non-metastatic counterparts.[68] Therefore, it would be easier for hybrid matrices embedded in polymer arrays to adhere to their surfaces, potentially increasing death rates. However, these hypothetical mechanisms remain elusive and warrant further investigation.

CONCLUSIONS:

We presented a comprehensive investigation into the self-organization of desmopressin and its association with sodium polystyrene sulfonate (NaPSS). Our findings, obtained from an extensive combination of sophisticated structural methods, indicate that desmopressin forms oligomeric aggregates at sub-millimolar concentrations and successfully associates with NaPSS. The information on self-aggregation had a direct impact, for example, leading to the optimization of synthesis conditions, where we have found a decrease in yield when concentrations above the critical aggregation point are used. Our findings show that this association leads to the formation of fibrillar arrangements, as indicated by SAXS and cryo-TEM data, where peptide chains appear organized as shown by fluorimetry and circular dichroism data. Additionally, the combination of atomic force microscopy with nano-infrared spectroscopy allowed us to show that desmopressin is embedded in the polymeric matrix, forming peptide-enriched domains. We also observed that the hybrid desmopressin/NaPSS materials are well tolerated by non-metastatic MCF-7 cells, while in metastatic MDA-MB-231 cells the ability to reduce metabolic activity is observed. These findings provide an initial indication that the addition of NaPSS to desmopressin likely does not induce the formation of toxic compounds.

The production of hybrid polymer-peptide matrices may offer several advantages for potential biomedical applications of these platforms. In the specific case of desmopressin, its association with NaPSS, a sodium-releasing agent, could be beneficial, as hyponatremia is its most serious side effect.[26] Furthermore, *in vivo* studies reported in the literature have shown that polymer association can potentially reduce the required dosage and improve the release time of drugs administered via nasal

sprays,[21,69,70] the most common method for desmopressin delivery. In the context of this study, both desmopressin and NaPSS are already used as commercially available medicines, having been validated in clinical trials. Therefore, starting with components that are already validated for medical use enhances the potential applications of the hybrid systems presented here and contributes to future developments that could translate into therapeutic use of these materials.

In summary, we anticipate that the results presented here will support further development of desmopressin-polymer platforms by detailing the roles of key chemical groups involved in the association, specifically the guanidinium groups of arginine in the peptide and the sulfonate moieties in NaPSS, demonstrating that the peptide is embedded within the polymer matrix. Our study also provides insights into the cellular interactions of these matrices, especially by showing that they are tolerated by MCF-7 cells but kill metastatic MDA-MB-231 cells. Considering the comprehensive nature of the work, presenting both physicochemical characterization through advanced methods and cell assay data, the findings represent a contribution to the literature on these promising platforms.

ACKNOWLEDGEMENTS:

This study has been mainly supported by the Sao Paulo Research Foundation, FAPESP, under grants #22/03056-6 and #23/18385-8 to ERS, #21/04885-3 to CRN, and #17/22047-0 to GM. The Brazilian Council for Scientific Research, CNPq, is acknowledged for grant # 409455/2018-0 (to ERS) and post-doctoral fellowship #402154/2022-3 (to RNB). CNPq and UNIFESP are acknowledged for a undergraduate fellowship granted to ABC through the PIBIC program. LRM thank FAPESP for a PhD fellowship (# 2019/19719-1). The Brazilian Foundation, Coordenação de Aperfeiçoamento de Pessoal de Nível Superior (CAPES) supported this study under grant PrInt 88881.311044/2018-00. ABC received a CAPES-PrInt fellowship to perform cryo-TEM experiments at the University Paris-Saclay (# 88887.978375/2024-00). The Brazilian Nanotechnology National Laboratory (LNNano) is acknowledged for granting access to TEM and AFM instruments under proposals: #TEM-24500 and #20220321, and we are grateful to Dr. Carlos Costa and Dr. Antonio Borges for assistance. We acknowledge SOLEIL for provision of synchrotron radiation facilities (proposals 20211309 and BAG

202111131), and we thank Aurélien Thureau for assistance in using the SWING beamline. Dr. Elisabetta Rosa (University of Naples Federico II) is acknowledged for help during preliminary SAXS measurements. IWH was supported by EPSRC Fellowship grant EP/V053396/1. We acknowledge Prof. Dr. Helena B. Nader, from Department of Biochemistry at EPM-UNIFESP, for contributing to the facility for performing the cell culture experiments. Cryo-TEM instrumentation used in this work was supported by the French State under the France 2030 program (PhOM - Graduate School of Physics) with the reference # ANR-11-IDEX-0003.

AUTHOR CONTRIBUTIONS:

Conceptualization: E.R.S., C.R.N., and A.J.C.Q.; *Investigation*: A.B.C, R.N.B., J.D., A.J.C.Q., L.E.A.S., C.C.S, L.R.M. *Methodology*: E.R.S., A.J.C.Q., J.D., I.W.H., C.R.N., S.E.G.S., C.C.S., M.G.S.; *Validation*: C.C.S., M.G.S., S.E.G.S., L.E.A.S., J.D., L.R.M., *Supervision*: E.R.S., A.J.C.Q., C.R.N., I.W.H., G.T., G.M. *Formal analysis*: A.B.C., E.R.S., R.N.B., A.J.C.Q., C.R.N., G.T., I.W.H. *Project Administration*: E.R.S., C.R.N., A.J.C.Q., *Writing:* A.B.C., R.N.B., A.J.C.Q., C.R.N., E.R.S. *Funding acquisition*: E.R.S., C.R.N., G.M., I.W.H., G.T.

REFERENCES

(1) Shu, J. Y.; Panganiban, B.; Xu, T. Peptide-Polymer Conjugates: From Fundamental Science to Application. *Annu. Rev. Phys. Chem.* **2013**, *64*, 631–657. https://doi.org/10.1146/annurev-physchem-040412-110108.

(2) Radvar, E.; Azevedo, H. S. Supramolecular Peptide/Polymer Hybrid Hydrogels for Biomedical Applications. *Macromol. Biosci.* **2019**, *19* (1, SI). https://doi.org/10.1002/mabi.201800221.

(3) Drucker, D. J. Advances in Oral Peptide Therapeutics. *Nat. Rev. Drug Discov.* **2020**, *19* (4), 277–289. https://doi.org/10.1038/s41573-019-0053-0.

(4) Bankir, L.; Bichet, D. G.; Morgenthaler, N. G. Vasopressin: Physiology, Assessment and Osmosensation. *J. Intern. Med.* **2017**, *282* (4), 284–297. https://doi.org/https://doi.org/10.1111/joim.12645.

(5) Christ-Crain, M.; Bichet, D. G.; Fenske, W. K.; Goldman, M. B.; Rittig, S.; Verbalis, J. G.; Verkman, A. S. Diabetes Insipidus. *Nat. Rev. Dis. Prim.* **2019**, *5* (1), 54. https://doi.org/10.1038/s41572-019-0103-2.

(6) Mutter, C. M.; Smith, T.; Menze, O.; Zakharia, M.; Nguyen, H. Diabetes Insipidus:

Pathogenesis, Diagnosis, and Clinical Management. *Cureus* **2021**, *13* (2), e13523–e13523. https://doi.org/10.7759/cureus.13523.

(7) Nevéus, T. Pathogenesis of Enuresis: Towards a New Understanding. *Int. J. Urol.* **2017**, *24* (3), 174–182. https://doi.org/https://doi.org/10.1111/iju.13310.

(8) Chung, E. Desmopressin and Nocturnal Voiding Dysfunction: Clinical Evidence and Safety Profile in the Treatment of Nocturia. *Expert Opin. Pharmacother.* **2018**, *19* (3), 291–298. https://doi.org/10.1080/14656566.2018.1429406.

(9) Franchini, M. The Use of Desmopressin as a Hemostatic Agent: A Concise Review. *Am. J. Hematol.* **2007**, *82* (8), 731–735. https://doi.org/10.1002/ajh.20940.

(10) Chin, X.; Teo, S. W.; Lim, S. T.; Ng, Y. H.; Han, H. C.; Yap, F. Desmopressin Therapy in Children and Adults: Pharmacological Considerations and Clinical Implications. *Eur. J. Clin. Pharmacol.* **2022**. https://doi.org/10.1007/s00228-022-03297-z.

(11) Mannucci, P. M. Desmopressin: An Historical Introduction. *Haemophilia* **2008**, *14 Suppl 1*, 1–4. https://doi.org/10.1111/j.1365-2516.2007.01609.x.

(12) Loomans, J. I.; Kruip, M. J. H. A.; Carcao, M.; Jackson, S.; van Velzen, A. S.; Peters, M.; Santagostino, E.; Platokouki, H.; Beckers, E.; Voorberg, J.; van der Bom, J. G.; Fijnvandraat, K. Desmopressin in Moderate Hemophilia A Patients: A Treatment Worth Considering. *Haematologica* **2018**, *103* (3), 550–557. https://doi.org/10.3324/haematol.2017.180059.

(13) Federici, A. B. The Use of Desmopressin in von Willebrand Disease: The Experience of the First 30 Years (1977–2007). *Haemophilia* **2008**, *14* (s1), 5–14. https://doi.org/https://doi.org/10.1111/j.1365-2516.2007.01610.x.

(14) Sobol, N. T.; Solernó, L. M.; Beltrán, B.; Vásquez, L.; Ripoll, G. V.; Garona, J.; Alonso, D. F. Anticancer Activity of Repurposed Hemostatic Agent Desmopressin on AVPR2-Expressing Human Osteosarcoma. *Exp. Ther. Med.* **2021**, *21* (6), 566. https://doi.org/10.3892/etm.2021.9998.

(15) Sasaki, H.; Klotz, L. H.; Sugar, L. M.; Kiss, A.; Venkateswaran, V. A Combination of Desmopressin and Docetaxel Inhibit Cell Proliferation and Invasion Mediated by Urokinase-Type Plasminogen Activator (UPA) in Human Prostate Cancer Cells. *Biochem. Biophys. Res. Commun.* **2015**, *464* (3), 848–854. https://doi.org/https://doi.org/10.1016/j.bbrc.2015.07.050.

(16) Ripoll, G. V; Garona, J.; Pifano, M.; Farina, H. G.; Gomez, D. E.; Alonso, D. F. Reduction of Tumor Angiogenesis Induced by Desmopressin in a Breast Cancer Model. *Breast Cancer Res. Treat.* **2013**, *142* (1), 9–18. https://doi.org/10.1007/s10549-013-2724-6.

(17) Weinberg, R. S.; Grecco, M. O.; Ferro, G. S.; Seigelshifer, D. J.; Perroni, N. V; Terrier, F. J.; Sánchez-Luceros, A.; Maronna, E.; Sánchez-Marull, R.; Frahm, I.; Guthmann, M. D.; Di Leo, D.; Spitzer, E.; Ciccia, G. N.; Garona, J.; Pifano, M.; Torbidoni, A. V; Gomez, D. E.; Ripoll, G. V; Gomez, R. E.; Demarco, I. A.; Alonso, D. F. A Phase II Dose-Escalation Trial of Perioperative Desmopressin (1-Desamino-8-d-Arginine Vasopressin) in Breast Cancer Patients. *Springerplus* **2015**, *4*, 428. https://doi.org/10.1186/s40064-015-1217-y.

(18) Iseas, S.; Roca, E. L.; O'Connor, J. M.; Eleta, M.; Sanchez-Luceros, A.; Di Leo, D.; Tinelli, M.; Fara, M. L.; Spitzer, E.; Demarco, I. A.; Ripoll, G. V; Pifano, M.; Garona, J.; Alonso, D. F. Administration of the Vasopressin Analog Desmopressin for the Management of Bleeding in Rectal Cancer Patients: Results of a Phase I/II Trial. *Invest. New Drugs* **2020**, *38* (5), 1580–1587. https://doi.org/10.1007/s10637-020-00914-5.

(19) Pena, A.; Murat, B.; Trueba, M.; Ventura, M. A.; Wo, N. C.; Szeto, H. H.; Cheng, L. L.; Stoev, S.; Guillon, G.; Manning, M. Design and Synthesis of the First Selective Agonists for the Rat Vasopressin V1b Receptor: Based on Modifications of Deamino-[Cys]Arginine Vasopressin at Positions 4 and 8. *J. Med. Chem.* **2007**, *50* (4), 835–847. https://doi.org/10.1021/jm060928n.

(20) Mannucci, P. M.; Aberg, M.; Nilsson, I. M.; Robertson, B. Mechanism of Plasminogen Activator and Factor VIII Increase after Vasoactive Drugs. *Br. J. Haematol.* **1975**, *30* (1), 81–93. https://doi.org/10.1111/j.1365-2141.1975.tb00521.x.

(21) Balducci, A. G.; Ferraro, L.; Bortolotti, F.; Nastruzzi, C.; Colombo, P.; Sonvico, F.; Russo, P.; Colombo, G. Antidiuretic Effect of Desmopressin Chimera Agglomerates by Nasal Administration in Rats. *Int. J. Pharm.* **2013**, *440* (2), 154–160. https://doi.org/https://doi.org/10.1016/j.ijpharm.2012.09.049.

(22) Libster, D.; Aserin, A.; Garti, N. Interactions of Biomacromolecules with Reverse Hexagonal Liquid Crystals: Drug Delivery and Crystallization Applications. *J Colloid Interface Sci* **2011**, *356* (2), 375–386. https://doi.org/S0021-9797(11)00063-4 [pii]10.1016/j.jcis.2011.01.047.

(23) Ilan, E.; Amselem, S.; Weisspapir, M.; Schwarz, J.; Yogev, A.; Zawoznik, E.; Friedman, D. Improved Oral Delivery of Desmopressin via a Novel Vehicle: Mucoadhesive Submicron Emulsion. *Pharm. Res.* **1996**, *13* (7), 1083–1087. https://doi.org/10.1023/a:1016023111248.

(24) Chevalier, M. T.; Garona, J.; Sobol, N. T.; Farina, H. G.; Alonso, D. F.; Álvarez, V. A. In Vitro and in Vivo Evaluation of Desmopressin-Loaded Poly(D,L-Lactic-Co-Glycolic Acid) Nanoparticles for Its Potential Use in Cancer Treatment. *Nanomedicine (Lond).* **2018**, *13* (22), 2835–2849. https://doi.org/10.2217/nnm-2018-0065.

(25) Sterns, R. H.; Grieff, M.; Bernstein, P. L. Treatment of Hyperkalemia: Something Old, Something New. *Kidney Int.* **2016**, *89* (3), 546–554. https://doi.org/https://doi.org/10.1016/j.kint.2015.11.018.

(26) Fralick, M.; Schneeweiss, S.; Wallis, C. J. D.; Jung, E. H.; Kesselheim, A. S. Desmopressin and the Risk of Hyponatremia: A Population-Based Cohort Study. *PLOS Med.* **2019**, *16* (10), 1–11. https://doi.org/10.1371/journal.pmed.1002930.

(27) Merrifield, B. Solid-Phase Synthesis. *Science.* **1986**, *232* (4748), 341–347.

(28) Hou, W.; Zhang, X.; Liu, C.-F. Progress in Chemical Synthesis of Peptides and Proteins. *Trans. Tianjin Univ.* **2017**, *23* (5), 401–419. https://doi.org/10.1007/s12209-017-0068-8.

(29) Palomo, J. M. Solid-Phase Peptide Synthesis: An Overview Focused on the Preparation of Biologically Relevant Peptides. *RSC Adv.* **2014**, *4* (62), 32658–32672. https://doi.org/10.1039/C4RA02458C.

(30) Jubilut, G. N.; Cilli, E. M.; Tominaga, M.; Miranda, A.; Okada, Y.; Nakaie, C. R. Evaluation of the Trifluoromethanosulfonic Acid/Trifluoroacetic Acid/Thioanisole Cleavage Procedure for Application in Solid-Phase Peptide Synthesis. *Chem. Pharm. Bull. (Tokyo).* **2001**, *49* (9), 1089–1092. https://doi.org/10.1248/cpb.49.1089.

(31) Bressler, I.; Kohlbrecher, J.; Thunemann, A. F. SASfit: A Tool for Small-Angle Scattering Data Analysis Using a Library of Analytical Expressions. *J. Appl. Crystallogr.* **2015**, *48* (5), 1587–1598. https://doi.org/doi:10.1107/S1600576715016544.

(32) West, R. M. Best Practice in Statistics: Use the Welch t-Test When Testing the Difference between Two Groups. *Ann. Clin. Biochem.* **2021**, *58* (4), 267–269. https://doi.org/10.1177/0004563221992088.

(33) de Mello, L. R.; Porosk, L.; Lourenço, T. C.; Garcia, B. B. M.; Costa, C. A. R.; Han, S. W.; de Souza, J. S.; Langel, Ü.; da Silva, E. R. Amyloid-like Self-Assembly of a Hydrophobic Cell-Penetrating Peptide and Its Use as a Carrier for Nucleic Acids. *ACS Appl. Bio Mater.* **2021**, *4* (8), 6404–6416. https://doi.org/10.1021/acsabm.1c00601.

(34) Hawe, A.; Sutter, M.; Jiskoot, W. Extrinsic Fluorescent Dyes as Tools for Protein Characterization. *Pharm. Res.* **2008**, *25* (7), 1487–1499. https://doi.org/10.1007/s11095-007-9516-9.

(35) Miles, A. J.; Janes, R. W.; Wallace, B. A. Tools and Methods for Circular Dichroism Spectroscopy of Proteins: A Tutorial Review. *Chem. Soc. Rev.* **2021**, *50* (15), 8400–8413. https://doi.org/10.1039/d0cs00558d.

(36) Greenfield, N. J. Using Circular Dichroism Spectra to Estimate Protein Secondary Structure. *Nat. Protoc.* **2006**, *1* (6), 2876–2890. https://doi.org/10.1038/nprot.2006.202.

(37) Walse, B.; Kihlberg, J.; Drakenberg, T. Conformation of Desmopressin, an Analogue of the Peptide Hormone Vasopressin, in Aqueous Solution as Determined by NMR Spectroscopy. *Eur. J. Biochem.* **1998**, *252* (3), 428–440. https://doi.org/10.1046/j.1432-1327.1998.2520428.x.

(38) Wang, J.; Breslow, E.; Sykes, B. D. Differential Binding of Desmopressin and Vasopressin to Neurophysin-II *. *J. Biol. Chem.* **1996**, *271* (49), 31354–31359. https://doi.org/10.1074/jbc.271.49.31354.

(39) Brahms, S.; Brahms, J.; Spach, G.; Brack, A. Identification of Beta,Beta-Turns and Unordered Conformations in Polypeptide-Chains by Vacuum Uv Circular-Dichroism. *Proc. Natl. Acad. Sci. U. S. A.* **1977**, *74* (8), 3208–3212. https://doi.org/DOI 10.1073/pnas.74.8.3208.

(40) Nordén, B.; Rodger, A.; Dafforn, T.; Royal Society of Chemistry (Great Britain). *Linear Dichroism and Circular Dichroism : A Textbook on Polarized-Light Spectroscopy*; Royal Society of Chemistry: Cambridge, 2010.

(41) Nilsson, M. R. Techniques to Study Amyloid Fibril Formation in Vitro. *Methods* **2004**, *34* (1), 151–160.

(42) Verma, S.; Ravichandiran, V.; Ranjan, N. Beyond Amyloid Proteins: Thioflavin T in Nucleic Acid Recognition. *Biochimie* **2021**, *190*, 111–123. https://doi.org/https://doi.org/10.1016/j.biochi.2021.06.003.

(43) Hu, Y.; Zandi, R.; Anavitarte, A.; Knobler, C. M.; Gelbart, W. M. Packaging of a Polymer by a Viral Capsid: The Interplay between Polymer Length and Capsid Size. *Biophys. J.* **2008**, *94* (4), 1428–1436. https://doi.org/10.1529/biophysj.107.117473.

(44) Asor, R.; Singaram, S. W.; Levi-Kalisman, Y.; Hagan, M. F.; Raviv, U. Effect of Ionic Strength on the Assembly of Simian Vacuolating Virus Capsid Protein around Poly(Styrene Sulfonate). *Eur. Phys. J. E* **2023**, *46* (11), 107. https://doi.org/10.1140/epje/s10189-023-00363-x.

(45) Marichal, L.; Gargowitsch, L.; Rubim, R. L.; Sizun, C.; Kra, K.; Bressanelli, S.; Dong, Y.; Panahandeh, S.; Zandi, R.; Tresset, G. Relationships between RNA Topology and Nucleocapsid Structure in a Model Icosahedral Virus. *Biophys. J.* **2021**, *120* (18), 3925–3936. https://doi.org/10.1016/j.bpj.2021.08.021.

(46) Pedersen, J. S. Analysis of Small-Angle Scattering Data from Colloids and Polymer Solutions: Modeling and Least-Squares Fitting. *Adv. Colloid Interface Sci.* **1997**, *70* (0), 171–210. https://doi.org/http://dx.doi.org/10.1016/S0001-8686(97)00312-6.

(47) Prevost, S.; Lopian, T.; Pleines, M.; Diat, O.; Zemb, T. Small-Angle Scattering and Morphologies of Ultra-Flexible Microemulsions. *J. Appl. Crystallogr.* **2016**, *49* (6), 2063–2072. https://doi.org/10.1107/S1600576716016150.

(48) De Mello, L. R.; Hamley, I. W.; Castelletto, V.; Garcia, B. B. M.; Han, S. W.; De Oliveira, C. L. P.; Da Silva, E. R. Nanoscopic Structure of Complexes Formed between DNA and the Cell-Penetrating Peptide Penetratin. *J. Phys. Chem. B* **2019**, *123* (42), 8861–8871. https://doi.org/10.1021/acs.jpcb.9b05512.

(49) Hammouda, B. A New Guinier-Porod Model. *J. Appl. Crystallogr.* **2010**, *43* (4), 716–719. https://doi.org/doi:10.1107/S0021889810015773.

(50) Dazzi, A.; Prater, C. B. AFM-IR: Technology and Applications in Nanoscale Infrared Spectroscopy and Chemical Imaging. *Chem. Rev.* **2017**, *117* (7), 5146–5173. https://doi.org/10.1021/acs.chemrev.6b00448.

(51) Dazzi, A.; Glotin, F.; Carminati, R. Theory of Infrared Nanospectroscopy by Photothermal Induced Resonance. *J. Appl. Phys.* **2010**, *107* (12), 124519. https://doi.org/10.1063/1.3429214.

(52) V. D. dos Santos, A. C.; Hondl, N.; Ramos-Garcia, V.; Kuligowski, J.; Lendl, B.; Ramer, G. AFM-IR for Nanoscale Chemical Characterization in Life Sciences: Recent Developments and Future Directions. *ACS Meas. Sci. Au* **2023**, *3* (5), 301–314. https://doi.org/10.1021/acsmeasuresciau.3c00010.

(53) Schwartz, J. J.; Jakob, D. S.; Centrone, A. A Guide to Nanoscale IR Spectroscopy: Resonance Enhanced Transduction in Contact and Tapping Mode AFM-IR. *Chem. Soc. Rev.* **2022**, *51* (13), 5248–5267. https://doi.org/10.1039/D2CS00095D.

(54) Mello, L. R.; Hamley, I. W.; Miranda, A.; Alves, W. A.; Silva, E. R. β-Sheet Assembly in Amyloidogenic Glutamic Acid Nanostructures: Insights from X-Ray Scattering and Infrared Nanospectroscopy. *J. Pept. Sci.* **2019**, *25* (6), e3170. https://doi.org/10.1002/psc.3170.

(55) Barth, A. Infrared Spectroscopy of Proteins. *Biochim. Biophys. Acta - Bioenerg.* **2007**, *1767* (9), 1073–1101. https://doi.org/https://doi.org/10.1016/j.bbabio.2007.06.004.

(56) Kong, J.; Yu, S. Fourier Transform Infrared Spectroscopic Analysis of Protein Secondary Structures. *Acta Biochim. Biophys. Sin. (Shanghai).* **2007**, *39* (8), 549–559. https://doi.org/10.1111/j.1745-7270.2007.00320.x.

(57) Balding, P.; Borrelli, R.; Volkovinsky, R.; Russo, P. S. Physical Properties of Sodium Poly(Styrene Sulfonate): Comparison to Incompletely Sulfonated Polystyrene. *Macromolecules* **2022**, *55* (5), 1747–1762. https://doi.org/10.1021/acs.macromol.1c01065.

(58) Yang, J. C.; Jablonsky, M. J.; Mays, J. W. NMR and FT-IR Studies of Sulfonated Styrene-Based Homopolymers and Copolymers. *Polymer (Guildf).* **2002**, *43* (19), 5125–5132. https://doi.org/https://doi.org/10.1016/S0032-3861(02)00390-7.

(59) Yuan, C.; Xing, R.; Cui, J.; Fan, W.; Li, J.; Yan, X. Multistep Desolvation as a Fundamental Principle Governing Peptide Self-Assembly Through Liquid–Liquid Phase Separation. *CCS Chem.* **2024**, *6* (1), 255–265. https://doi.org/10.31635/ccschem.023.202302990.

(60) Yuan, C.; Ji, W.; Xing, R.; Li, J.; Gazit, E.; Yan, X. Hierarchically Oriented Organization in Supramolecular Peptide Crystals. *Nat. Rev. Chem.* **2019**, *3* (10), 567–588. https://doi.org/10.1038/s41570-019-0129-8.

(61) Zhou, P.; Xing, R.; Li, Q.; Li, J.; Yuan, C.; Yan, X. Steering Phase-Separated Droplets to Control Fibrillar Network Evolution of Supramolecular Peptide Hydrogels. *Matter* **2023**. https://doi.org/https://doi.org/10.1016/j.matt.2023.03.029.

(62) Yuan, C.; Levin, A.; Chen, W.; Xing, R.; Zou, Q.; Herling, T. W.; Challa, P. K.; Knowles, T. P. J.; Yan, X. Nucleation and Growth of Amino Acid and Peptide Supramolecular Polymers through Liquid–Liquid Phase Separation. *Angew. Chemie Int. Ed.* **2019**, *58* (50), 18116–18123. https://doi.org/https://doi.org/10.1002/anie.201911782.

(63) Rotoli, B. M.; Visigalli, R.; Ferrari, F.; Ranieri, M.; Tamma, G.; Dall'Asta, V.; Barilli, A. Desmopressin Stimulates Nitric Oxide Production in Human Lung Microvascular Endothelial Cells. *Biomolecules* **2022**, *12* (3). https://doi.org/10.3390/biom12030389.

(64) Ripoll, G. V; Farina, H. G.; Yoshiji, H.; Gomez, D. E.; Alonso, D. F. Desmopressin Reduces Melanoma Lung Metastasis in Transgenic Mice Overexpressing Tissue Inhibitor of Metalloproteinases-1. *In Vivo* **2006**, *20* (6B), 881–885.

(65) Holliday, D. L.; Speirs, V. Choosing the Right Cell Line for Breast Cancer Research. *Breast Cancer Res.* **2011**, *13* (4), 215. https://doi.org/10.1186/bcr2889.

(66) Castelletto, V.; Edwards-Gayle, C. J. C.; Greco, F.; Hamley, I. W.; Seitsonen, J.; Ruokolainen, J. Self-Assembly, Tunable Hydrogel Properties, and Selective Anti-Cancer Activity of a Carnosine-Derived Lipidated Peptide. *ACS Appl. Mater. Interfaces* **2019**, *11* (37), 33573–33580. https://doi.org/10.1021/acsami.9b09065.

(67) Romero-Garcia, S.; Lopez-Gonzalez, J. S.; Báez-Viveros, J. L.; Aguilar-Cazares, D.; Prado-Garcia, H. Tumor Cell Metabolism: An Integral View. *Cancer Biol. Ther.* **2011**, *12* (11), 939–948. https://doi.org/10.4161/cbt.12.11.18140.

(68) Alibert, C.; Goud, B.; Manneville, J.-B. Are Cancer Cells Really Softer than Normal Cells? *Biol. Cell* **2017**, *109* (5), 167–189. https://doi.org/https://doi.org/10.1111/boc.201600078.

(69) Henriques, P.; Fortuna, A.; Doktorovová, S. Spray Dried Powders for Nasal Delivery: Process and Formulation Considerations. *Eur. J. Pharm. Biopharm.* **2022**, *176*, 1–20. https://doi.org/https://doi.org/10.1016/j.ejpb.2022.05.002.

(70) Wan, F.; Maltesen, M. J.; Bjerregaard, S.; Foged, C.; Rantanen, J.; Yang, M. Particle Engineering Technologies for Improving the Delivery of Peptide and Protein Drugs. *J. Drug Deliv. Sci. Technol.* **2013**, *23* (4), 355–363. https://doi.org/https://doi.org/10.1016/S1773-2247(13)50052-9.

ToC

Desmopressin and NaPSS self-assemble into β-sheet-enriched nanofibrils, selectively inhibit metastatic breast cancer cells, and highlight peptide-polymer therapeutic potential by integrating two clinically validated drugs into a novel hybrid matrix.